In: Algorithms for Synthetic Aperture Imaging XIV (Proc. SPIE 6569), SPIE Defense and Security Symposium, Orlando, FL, April 2007.

Joint Enhancement of Multichannel SAR Data

Naveen Ramakrishnan, Emre Ertin and Randolph L. Moses
The Ohio State University, Department of Electrical and Computer Engineering
2015 Neil Avenue, Columbus, OH - 43210, USA

ABSTRACT

In this paper we consider the problem of joint enhancement of multichannel Synthetic Aperture Radar (SAR) data. Previous work by Cetin and Karl introduced nonquadratic regularization methods for image enhancement using sparsity enforcing penalty terms. For multichannel data, independent enhancement of each channel is shown to degrade the relative phase information across channels that is useful for 3D reconstruction. We thus propose a method for joint enhancement of multichannel SAR data with joint sparsity constraints. We develop both a gradient-based and a Lagrange-Newton-based method for solving the joint reconstruction problem, and demonstrate the performance of the proposed methods on IFSAR height extraction problem from multi-elevation data.

Keywords: Non-quadratic regularization, Sparse reconstruction, SAR, IFSAR

1. INTRODUCTION

Synthetic Aperture Radar (SAR) is one of the most widely-used sensing technologies for object and scene recognition, due to its day/night and all-weather performance capabilities. Traditional SAR image formation entails Fourier processing of limited-angle, limited-bandwidth measurements to form a reflectivity image of the scene. Fourier processing has many advantages, namely linear processing, well-understood characteristics, and computational speed. However, Fourier processing of limited-extent data has inherent resolution limits[1]; in addition, Fourier processing generates significant sidelobe artifacts when some frequencies or measurement angles are denied or blocked.[2]

To address these resolution limits and artifact terms, nonlinear reconstruction techniques have been proposed.[3–5] In this paper we focus on a sparse-signal enhancement approach.[2,3] The basic idea is to reconstruct an image that is simultaneously in good agreement with the measured data, and is regularized by using some prior information; the most common prior information is that the reconstruction is *sparse* in some domain. SAR image reconstruction techniques of targets, using a sparse image regularization term, has been shown to provide enhanced resolution[2] and also significant robustness to missing data.[2] The sparseness term attempts to find a reconstructed image with a sparse number of large-amplitude pixels, to account for the simple prior knowledge that at high frequencies, most large-amplitude backscattering from many objects occurs at discrete scattering centers on the object.[6]

In this paper we consider similar SAR image reconstruction techniques when applied to multi-channel SAR data. Multi-channel SAR may arise from multiple polarization channel measurement or from multiple phase center measurements, such as in interferometric SAR (IFSAR). In IFSAR, the height of a scattering center (as measured from the slant plane) can be estimated from the phase difference between the corresponding pixels of two phase-coherent, high resolution SAR images with some elevation offset.[7] For many multi-channel data sets, the sparseness is expected to be the same for all the channels; for example, in IFSAR the high-amplitude pixels are expected to be in the same locations for all channels. In addition, the *relative phase* of the images across channels often contains important information, and it is important to preserve this relative phase in the reconstruction process. For example, the polarimetric properties of a scattering center in multi-polarization data, or the 3D location of a scattering center from two IFSAR images both depend on the relative phase.

Corresponding author: Randolph L. Moses, E-mail: moses.2@osu.edu. This material is based upon work supported by the Air Force Office of Scientific Research under Award No. FA9550-06-1-0324. Any opinions, findings, and conclusions or recommendations expressed in this publication are those of the authors and do not necessarily reflect the views of the Air Force.

For multi-channel data, one approach to reconstruction is to apply existing techniques *independently* for each channel. Such an approach neither enforces common sparsity nor preserves relative phase. Simulation results presented in Section 4 demonstrate that for IFSAR, independent reconstruction results in different large-amplitude pixels in each channel, and degrades relative phase across reconstructed images. To address these issues, we propose a joint reconstruction approach that places a joint sparseness constraint across multi-channel images. By constraining all reconstructed images to have the same large-amplitude pixels, the relative phase of the reconstructed images appears to be much better preserved than in the independent reconstruction case.

The remainder of the paper is organized as follows. Section 2 presents the system model and describes the independent enhancement problem. Section 3 introduces the joint-reconstruction problem and presents two solution techniques, a gradient-based technique and a Lagrange-Newton technique. Section 4 presents numerical examples that illustrates the effectiveness of the joint reconstruction technique as compared with independent channel reconstruction. Finally, Section 5 presents conclusions and discusses potential future work.

2. SYSTEM MODEL

In this section, we describe the system model considered and present the independent enhancement problem. For ease of explanation, the problem is developed for two SAR measurement apertures at closely-spaced elevations as used for IFSAR, although the problem applies to > 2 channels or other applications than IFSAR.

The ground-plane geometry for the spotlight-mode SAR is shown in Figure 1. We consider a linear path SAR at each of the two elevations with the same center azimuth angle. The reflected field from the ground patch is collected and processed to form the 2D complex reflectivity function $f(x, y)$ where x, y are the downrange and crossrange dimensions of the ground plane, respectively. The observation model for multiple spotlight-mode SAR measurements are represented as

$$\boldsymbol{g}_i = \boldsymbol{T}_i \boldsymbol{f}_i + \boldsymbol{w}_i, \quad i = 1, 2, \ldots, n \tag{1}$$

where each $N \times 1$ vector $\boldsymbol{g}_i$ is the SAR image formed from the ith channel measurements using *e.g.*, the polar-formatting method, $\boldsymbol{T}_i$ describes the point spread function of the imaging operator used in forming $\boldsymbol{g}_i$, $\boldsymbol{f}_i$ is the enhanced image for the ith channel, and $\boldsymbol{w}_i$ is a measurement noise vector, which is assumed to be complex additive white Gaussian noise. Here, N is the number of pixels in the SAR image.

In this paper, we assume $n = 2$ and that $\boldsymbol{g_1}$ and $\boldsymbol{g_2}$ are images formed at elevation angles ψ_1 and ψ_2 that are sufficiently closely-spaced so that IFSAR processing can be used to obtain the 3D reconstruction of objects in the scene.

2.1. Independent Enhancement

We assume that a pair of SAR images taken from two elevations ψ_1 and ψ_2 separated by $\triangle\psi \ll 1$ and from the same center azimuth angle are formed using the Polar Formatting Algorithm.[1] A method for enhancing the SAR images by introducing nonquadratic sparsity inducing terms has been discussed, where the point-enhanced SAR imaging is achieved by solving the following optimization problem,[2]

$$\boldsymbol{f_i} = \arg\min_{\boldsymbol{f}} \quad J_i(\boldsymbol{f}) \qquad i = 1, 2 \tag{2}$$

where $J_i(\boldsymbol{f})$ is given by,

$$J_i(\boldsymbol{f}) = \|\boldsymbol{g_i} - \boldsymbol{T_i}\boldsymbol{f}\|_2^2 + \lambda^2 \|\boldsymbol{f}\|_p^p \tag{3}$$

Each cost function J_i represents a tradeoff between choosing f_i to match the measured data in an ℓ_2-norm sense, and sparsity in the resulting image by minimizing the ℓ_p-norm of f_i for $p \leq 1$. The parameter λ^2 is chosen to weight the data-fitting and solution sparseness terms in the optimization problem. Typically, p is chosen between 0.7 and 1.[2]

For independent enhancement, the above optimization problem is solved for each of the images to form two point-enhanced SAR images corresponding to the elevations ψ_1 and ψ_2. Each enhancement involves solving an *unconstrained* optimization problem with $2N$ real variables $(\mathrm{Re}(\boldsymbol{f_i}), \mathrm{Im}(\boldsymbol{f_i}))$. For IFSAR, one expects that

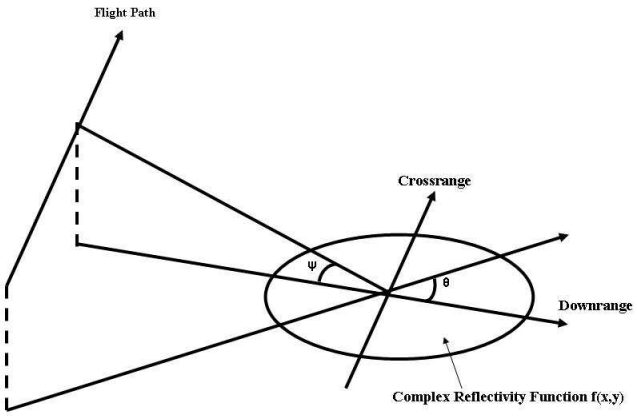

Figure 1. Spotlight SAR observation model.

the noiseless image has the property that large-amplitude pixels have the same amplitude and differing phase (assuming that there is a single scattering center in the range/crossrange cell). The height estimate $\hat{z_i}$ of the scattering center, as measured orthogonal to the slant-plane image, is given by,

$$\hat{z_j} = \frac{\lambda_c}{4\pi \triangle \psi} \arg((f_2)_j (f_1)_j^*) \qquad j = 1, ..., N \tag{4}$$

Note that the height estimate is linearly dependent on the relative phase between the image pixels. Thus, it is important that the phase difference across images be preserved during the enhancement process.

The independent enhancement technique has no component designed to preserve either amplitude or (relative) phase information across the individual images. In fact, since the methods produce sparse output images, it is often the case that scattering terms represented by several adjacent large-amplitude pixels in the conventional image are enhanced to produce fewer (possibly one) large-amplitude pixel in the enhanced image. Due to variations and noise in the individual images, it may well be that a different subset of large-amplitude pixels result from each enhancement process. In worst case, none of the large-amplitude pixels in $\boldsymbol{f_1}$ may have a similar large amplitude in image $\boldsymbol{f_2}$. In this case, IFSAR processing of independently-enhanced images is not possible.

3. JOINT ENHANCEMENT

In this section, we propose a method for jointly processing both images using sparsity inducing terms and also by including appropriate constraints which result in the reduction of the errors in the height estimates. Specifically, we impose an equal magnitude constraint, in which we jointly enhance the two SAR images such that their magnitudes are equal. Mathematically this can be represented as,

$$\arg \min_{\boldsymbol{f_1}, \boldsymbol{f_2}} \quad L(\boldsymbol{f_1}, \boldsymbol{f_2}) \tag{5}$$

subject to the constraint $|(f_1)_i| = |(f_2)_i| \qquad i = (1, ..., N)$
where $L(\boldsymbol{f_1}, \boldsymbol{f_2})$ is given by,

$$L(\boldsymbol{f_1}, \boldsymbol{f_2}) = \|\boldsymbol{g_1} - \boldsymbol{T_1 f_1}\|_2^2 + \|\boldsymbol{g_2} - \boldsymbol{T_2 f_2}\|_2^2 + \lambda_1^2 \|\boldsymbol{f_1}\|_p^p + \lambda_2^2 \|\boldsymbol{f_2}\|_p^p \tag{6}$$

The values of λ_1^2 and λ_2^2 are usually taken to be equal to λ^2, since both images are expected to be identically sparse. As before, the λ_i^2 parameters provide a relative weight to the data-fitting and sparseness terms in the optimization problem.

The above joint formulation leads to a *constrained* optimization problem with $4N$ real variables ($|\boldsymbol{f_1}|$, $|\boldsymbol{f_2}|$, $\boldsymbol{\phi_1}$ and $\boldsymbol{\phi_2}$), where $|\boldsymbol{f_i}|$, $|\boldsymbol{\phi_i}|$, are the vectors of element magnitudes and phases of the complex vector $\boldsymbol{f_i}$:

$$\boldsymbol{f_1} = e^{j\boldsymbol{\phi_1}}|\boldsymbol{f}| \qquad \boldsymbol{f_2} = e^{j\boldsymbol{\phi_2}}|\boldsymbol{f}| \tag{7}$$

where,

$$e^{j\boldsymbol{\phi_1}} = \text{diag}\left\{e^{j(\phi_1)_i}\right\}, \quad e^{j\boldsymbol{\phi_2}} = \text{diag}\left\{e^{j(\phi_2)_i}\right\}, \quad i = 1, 2, ..., N \tag{8}$$

are diagonal matrices and $(\phi_1)_i$, $(\phi_2)_i \quad i = 1, 2, ..., N$ are the set of angles at each pixel of $\boldsymbol{f}_1$ and $\boldsymbol{f}_2$ respectively. This is compared to two unconstrained optimizations with $2N$ real variables each resulting from (2). In order to avoid the difficulty of differentiating the ℓ_p-norm terms near zero, we approximate them by[3]

$$\|\boldsymbol{f_1}\|_p^p \approx \sum_{i=1}^{N} (|(f_1)_i|^2 + \epsilon)^{\frac{p}{2}}, \quad \|\boldsymbol{f_2}\|_p^p \approx \sum_{i=1}^{N} (|(f_2)_i|^2 + \epsilon)^{\frac{p}{2}} \tag{9}$$

where ϵ is a small positive constant. The following subsections develop two methods to solve this joint optimization problem.

3.1. Gradient Descent Method

One solution to (5) is obtained by including the equal magnitude constraint in the cost function itself. This is accomplished by forcing the enhanced images to have the same magnitudes, i.e. $|(f_1)_i| = |(f_2)_i| = |(f)_i|$ for $i = 1, \ldots, N$, which we denote with the compact notation $|\boldsymbol{f_1}| = |\boldsymbol{f_2}| = |\boldsymbol{f}|$. With this formulation, the number of unknowns in the cost function is decreased from $4N$ to $3N$ real variables, *i.e.*, we minimize the cost function $L(\boldsymbol{f_1}, \boldsymbol{f_2})$ with respect to the $3N \times 1$ vector $\boldsymbol{\theta}$ given by,

$$\boldsymbol{\theta} = \begin{bmatrix} |\boldsymbol{f}| \\ \boldsymbol{\phi_1} \\ \boldsymbol{\phi_2} \end{bmatrix}$$

We propose to use the gradient descent method for this purpose and hence find the gradient of $L(\boldsymbol{f_1}, \boldsymbol{f_2})$ with respect to $\boldsymbol{\theta}$. The gradient vector after sufficient simplifications is given by,

$$\nabla L_{\boldsymbol{\theta}} \quad = \quad \begin{bmatrix} \nabla L_{|\boldsymbol{f}|} \\ \nabla L_{\boldsymbol{\phi_1}} \\ \nabla L_{\boldsymbol{\phi_2}} \end{bmatrix} \tag{10}$$

where,

$$\begin{aligned} \nabla L_{|\boldsymbol{f}|} &= 2\text{Re}[-\boldsymbol{S_1}^H \boldsymbol{g_1} - \boldsymbol{S_2}^H \boldsymbol{g_2} + (\boldsymbol{S_1}^H \boldsymbol{S_1} + \boldsymbol{S_2}^H \boldsymbol{S_2})|\boldsymbol{f}|] + 2\lambda^2 \boldsymbol{\Lambda}|\boldsymbol{f}| \\ \nabla L_{\boldsymbol{\phi_1}} &= 2\text{Re}[j\boldsymbol{F_1}^H \boldsymbol{T_1}^H \boldsymbol{g_1} - j\boldsymbol{F_1}^H \boldsymbol{T_1}^H \boldsymbol{T_1} \boldsymbol{f_1}] \\ \nabla L_{\boldsymbol{\phi_2}} &= 2\text{Re}[j\boldsymbol{F_2}^H \boldsymbol{T_2}^H \boldsymbol{g_2} - j\boldsymbol{F_2}^H \boldsymbol{T_2}^H \boldsymbol{T_2} \boldsymbol{f_2}] \end{aligned} \tag{11}$$

and where,

$$\begin{aligned} \boldsymbol{S_1} &= \boldsymbol{T_1} e^{j\boldsymbol{\phi_1}}, \quad \boldsymbol{S_2} = \boldsymbol{T_2} e^{j\boldsymbol{\phi_2}} \\ \boldsymbol{F_1} &= \text{diag}\Big\{(f_1)_i\Big\}, \quad \boldsymbol{F_2} = \text{diag}\Big\{(f_2)_i\Big\}, \\ \boldsymbol{\Lambda} &= \text{diag}\left\{\frac{1}{(|(f)_i|^2 + \epsilon)^{1-\frac{p}{2}}}\right\} \quad i = 1, 2, ..., N \end{aligned} \tag{12}$$

The gradient vector is used to update the value of $\boldsymbol{\theta}$.

$$\boldsymbol{\theta}^{k+1} \quad = \quad \boldsymbol{\theta}^k + \gamma \nabla L_{\boldsymbol{\theta}} \tag{13}$$

where γ is a user-selected step size. The iteration is initialized by $|\boldsymbol{f}| = \frac{|\boldsymbol{g_1}|+|\boldsymbol{g_2}|}{2}$ and the initial phase angles are set to be the same as the observed phase angles, i.e. those of $\boldsymbol{g_1}$ and $\boldsymbol{g_2}$. These iterations are carried out until the convergence criteria

$$\frac{\|\boldsymbol{f_1}^{k+1} - \boldsymbol{f_1}^{k}\|}{\|\boldsymbol{f_1}^{k}\|} < \delta \quad \text{and} \quad \frac{\|\boldsymbol{f_2}^{k+1} - \boldsymbol{f_2}^{k}\|}{\|\boldsymbol{f_2}^{k}\|} < \delta$$

are met, for some user-selected $\delta > 0$. One main advantage of the gradient descent method is that it ensures that the final images $\boldsymbol{f_1}$ and $\boldsymbol{f_2}$ have pixels with exactly the same magnitudes, since the constraint is directly included in the cost function.

3.2. Lagrange-Newton Method

The Lagrange-Newton method is used for numerous nonlinear control optimization problems. In this method, the constraints are included in the cost function using the Lagrangian and the resulting function is optimized using quasi-Newton method. The optimization problem in this case becomes,

$$\min_{\boldsymbol{f_1},\boldsymbol{f_2}} \max_{\boldsymbol{\beta}} L(\boldsymbol{f_1}, \boldsymbol{f_2}, \boldsymbol{\beta}) \tag{14}$$

where, $\boldsymbol{\beta} = [\beta_1, \ldots, \beta_N]^T$ and

$$L(\boldsymbol{f_1}, \boldsymbol{f_2}, \boldsymbol{\beta}) = \|\boldsymbol{g_1} - \boldsymbol{T_1 f_1}\|_2^2 + \|\boldsymbol{g_2} - \boldsymbol{T_2 f_2}\|_2^2 + \lambda_1^2 \|\boldsymbol{f_1}\|_p^p + \lambda_2^2 \|\boldsymbol{f_2}\|_p^p + \sum_{i=1}^{N} \beta_i (|(f_1)_i|^2 - |(f_2)_i|^2) \tag{15}$$

The constraint has been included in the cost function and β_is are the Lagrange multipliers which will also be taken as parameters to be optimized.

The goal is to minimize the function given by the equation (15). The partial derivatives of $L(\boldsymbol{f_1}, \boldsymbol{f_2})$ are with respect to two complex vectors and hence has to be taken with respect to the real and imaginary components separately and then combined to form a complex vector. By doing this and simplifying the first partial derivatives with respect to $\boldsymbol{f_1}, \boldsymbol{f_2}$ and $\boldsymbol{\beta}$, we find

$$\begin{aligned} \nabla L(\boldsymbol{f_1}, \boldsymbol{f_2})_{\boldsymbol{f_1}} &= [2\boldsymbol{T_1}^H \boldsymbol{T_1} + p\lambda_1^2 \boldsymbol{\Lambda_1} + 2\boldsymbol{B}]\boldsymbol{f_1} - 2\boldsymbol{T_1}^H \boldsymbol{g_1} \\ \nabla L(\boldsymbol{f_1}, \boldsymbol{f_2})_{\boldsymbol{f_2}} &= [2\boldsymbol{T_2}^H \boldsymbol{T_2} + p\lambda_2^2 \boldsymbol{\Lambda_2} - 2\boldsymbol{B}]\boldsymbol{f_2} - 2\boldsymbol{T_2}^H \boldsymbol{g_2} \end{aligned} \tag{16}$$

where the matrices $\boldsymbol{B}, \boldsymbol{\Lambda_1}$ and $\boldsymbol{\Lambda_2}$ are given by,

$$\boldsymbol{B} = \operatorname{diag}\Big\{\beta_i\Big\}, \quad \boldsymbol{\Lambda_1} = \operatorname{diag}\left\{\frac{1}{(|(f_1)_i|^2 + \epsilon)^{1-\frac{p}{2}}}\right\} \quad \boldsymbol{\Lambda_2} = \operatorname{diag}\left\{\frac{1}{(|(f_2)_i|^2 + \epsilon)^{1-\frac{p}{2}}}\right\} \quad i = 1, 2, ..., N \tag{17}$$

and the gradient with respect to each β_i gives the constraint $|(f_1)_i| = |(f_2)_i| = |(f)_i|$ which, when substituted into (17), yields $\boldsymbol{\Lambda_1} = \boldsymbol{\Lambda_2} = \boldsymbol{\Lambda}$. Thus, the equations (16) become

$$\begin{aligned} \nabla L(\boldsymbol{f_1}, \boldsymbol{f_2})_{\boldsymbol{f_1}} &= [2\boldsymbol{T_1}^H \boldsymbol{T_1} + p\lambda^2 \boldsymbol{\Lambda} + 2\boldsymbol{B}]\boldsymbol{f_1} - 2\boldsymbol{T_1}^H \boldsymbol{g_1} \\ \nabla L(\boldsymbol{f_1}, \boldsymbol{f_2})_{\boldsymbol{f_2}} &= [2\boldsymbol{T_2}^H \boldsymbol{T_2} + p\lambda^2 \boldsymbol{\Lambda} - 2\boldsymbol{B}]\boldsymbol{f_2} - 2\boldsymbol{T_2}^H \boldsymbol{g_2} \end{aligned} \tag{18}$$

To find vectors $\boldsymbol{f_1}, \boldsymbol{f_2}$ which minimize (15) we set (18) to zero which further requires us to solve the following set of equations with the constraint that both $\boldsymbol{f_1}$ and $\boldsymbol{f_2}$ must have the same magnitude in each of their components.

$$\begin{aligned} [2\boldsymbol{T_1}^H \boldsymbol{T_1} + p\lambda^2 \boldsymbol{\Lambda} + 2\boldsymbol{B}]\boldsymbol{f_1} &= 2\boldsymbol{T_1}^H \boldsymbol{g_1} \\ [2\boldsymbol{T_2}^H \boldsymbol{T_2} + p\lambda^2 \boldsymbol{\Lambda} - 2\boldsymbol{B}]\boldsymbol{f_2} &= 2\boldsymbol{T_2}^H \boldsymbol{g_2} \end{aligned} \tag{19}$$

For solving these set of equations, along with the β_is as parameters, iterative methods such as the Conjugate Gradient method can be used.[8] But with direct implementation, it is not possible to ensure that the β_is remain

real-valued. Instead, we implement the real and imaginary parts of equations (19) separately, along with the (real) equation for $\boldsymbol{\beta}$. This gives:

$$\boldsymbol{M}\Delta\boldsymbol{x} = \boldsymbol{a} \tag{20}$$

where,

$$\boldsymbol{M} = \begin{bmatrix} \boldsymbol{M_{11}} & 0 & 2\left[\begin{array}{c}\boldsymbol{D_{R1}}\\ \hline \boldsymbol{D_{I1}}\end{array}\right] \\ 0 & \boldsymbol{M_{22}} & -2\left[\begin{array}{c}\boldsymbol{D_{R2}}\\ \hline \boldsymbol{D_{I2}}\end{array}\right] \\ 2\left[\begin{array}{c|c}\boldsymbol{D_{R1}} & \boldsymbol{D_{I1}}\end{array}\right] & -2\left[\begin{array}{c|c}\boldsymbol{D_{R2}} & \boldsymbol{D_{I2}}\end{array}\right] & 0 \end{bmatrix} \tag{21}$$

$$\boldsymbol{M_{11}} = \boldsymbol{R_1}^H\boldsymbol{R_1} + \left[\begin{array}{c|c}\boldsymbol{\Lambda} & 0\\ \hline 0 & \boldsymbol{\Lambda}\end{array}\right] + 2\left[\begin{array}{c|c}\boldsymbol{B} & 0\\ \hline 0 & \boldsymbol{B}\end{array}\right] \qquad \boldsymbol{M_{22}} = \boldsymbol{R_2}^H\boldsymbol{R_2} + \left[\begin{array}{c|c}\boldsymbol{\Lambda} & 0\\ \hline 0 & \boldsymbol{\Lambda}\end{array}\right] - 2\left[\begin{array}{c|c}\boldsymbol{B} & 0\\ \hline 0 & \boldsymbol{B}\end{array}\right]$$

$$\boldsymbol{D_{R1}} = \mathrm{diag}\{\mathrm{Re}(\boldsymbol{f_1})\}, \quad \boldsymbol{D_{I1}} = \mathrm{diag}\{\mathrm{Im}(\boldsymbol{f_1})\}, \quad \boldsymbol{D_{R2}} = \mathrm{diag}\{\mathrm{Re}(\boldsymbol{f_2})\}, \quad \boldsymbol{D_{I1}} = \mathrm{diag}\{\mathrm{Im}(\boldsymbol{f_2})\}$$

$$\Delta\boldsymbol{x} = \begin{bmatrix} \Delta\mathrm{Re}(\boldsymbol{f_1}) \\ \Delta\mathrm{Im}(\boldsymbol{f_1}) \\ \Delta\mathrm{Re}(\boldsymbol{f_1}) \\ \Delta\mathrm{Im}(\boldsymbol{f_1}) \\ \Delta\boldsymbol{\beta} \end{bmatrix}$$

$$\boldsymbol{a} = \begin{bmatrix} -\mathrm{Re}\{[2\boldsymbol{T_1}^H\boldsymbol{T_1} + p\lambda^2\boldsymbol{\Lambda} + 2\boldsymbol{B}]\boldsymbol{f_1} - 2\boldsymbol{T_1}^H\boldsymbol{g_1}\} \\ -\mathrm{Im}\{[2\boldsymbol{T_1}^H\boldsymbol{T_1} + p\lambda^2\boldsymbol{\Lambda} + 2\boldsymbol{B}]\boldsymbol{f_1} - 2\boldsymbol{T_1}^H\boldsymbol{g_1}\} \\ -\mathrm{Re}\{[2\boldsymbol{T_2}^H\boldsymbol{T_2} + p\lambda^2\boldsymbol{\Lambda} - 2\boldsymbol{B}]\boldsymbol{f_2} - 2\boldsymbol{T_2}^H\boldsymbol{g_2}\} \\ -\mathrm{Im}\{[2\boldsymbol{T_2}^H\boldsymbol{T_2} + p\lambda^2\boldsymbol{\Lambda} - 2\boldsymbol{B}]\boldsymbol{f_2} - 2\boldsymbol{T_2}^H\boldsymbol{g_2}\} \\ -|\boldsymbol{f_1}|^2 + |\boldsymbol{f_2}|^2 \end{bmatrix} \tag{22}$$

and the matrices $\boldsymbol{R_1}$, $\boldsymbol{R_2}$ are given by,

$$\boldsymbol{R_1} = \begin{bmatrix} \mathrm{Re}(\boldsymbol{T_1}) & \mathrm{Im}(\boldsymbol{T_1}) \\ -\mathrm{Im}(\boldsymbol{T_1}) & \mathrm{Re}(\boldsymbol{T_1}) \end{bmatrix} \qquad \boldsymbol{R_2} = \begin{bmatrix} \mathrm{Re}(\boldsymbol{T_2}) & \mathrm{Im}(\boldsymbol{T_2}) \\ -\mathrm{Im}(\boldsymbol{T_2}) & \mathrm{Re}(\boldsymbol{T_2}) \end{bmatrix} \tag{23}$$

Thus, the $3N$ complex equations have been rewritten as $5N$ real equations so that the constraint on the β_is that they must be real is easily satisfied. The matrix equation (20) cannot be iteratively solved using the Conjugate Gradient method since the matrix $\boldsymbol{M}$ is not guaranteed to be positive definite. We instead solve this equation using the minimum residual method, which requires the matrix $\boldsymbol{M}$ to be symmetric but not positive definite

The implementation of the Lagrange-Newton method requires two iterations, an outer iteration for updating the $5N$ variables and an inner iteration for solving the matrix equation using minimum residual method. This is done iteratively until the stopping criterion

$$\frac{\|\boldsymbol{f_1}^{k+1} - \boldsymbol{f_1}^{k}\|}{\|\boldsymbol{f_1}^{k}\|} < \delta, \quad \frac{\|\boldsymbol{f_2}^{k+1} - \boldsymbol{f_2}^{k}\|}{\|\boldsymbol{f_2}^{k}\|} < \delta \quad \text{and} \quad \frac{\|\boldsymbol{\beta}^{k+1} - \boldsymbol{\beta}^{k}\|}{\|\boldsymbol{\beta}^{k}\|} < \delta$$

is met for some user-selected $\delta > 0$.

The primary advantage of the Lagrange-Newton method, over the Gradient Descent solution discussed previously, is that the Lagrange-Newton method has quadratic convergence. On the other hand, the computation involves a larger number of parameters. There does not seem to be a definitive statement that one approach is better than the other in all cases, and characterization of their relative performance is a subject of ongoing research.

4. SIMULATION RESULTS

We illustrate the performances of the proposed joint approach using the synthetic multi-elevation data. We simulate four point scatterers in the scene at the (x, y, z) positions given by: (0,0,0), (0,3,0), (-2,-2,0) and (1,1,2) meters, and each with unit amplitude. We simulate two linear flight path apertures, with center elevations of 29.5° and 29.57°; these are close enough in elevation to permit IFSAR processing for scattering center height estimation. Both apertures are 20° wide and centered at 0°. The center frequency and bandwidth of the SAR system are 10GHz, 1GHz respectively and the images are formed over an azimuth width of 20°. Complex white Gaussian noise is added to the phase history data such that the peak SNR of the scatterers in the image is 21dB. Relative phase angles for image domain pixels within the top 35 dB are also plotted.

Figure 2 shows the resulting SAR images using the polar format algorithm for image formation, using a hamming window to reduce sidelobe artifacts. Also shown is the relative phase for pixels that are within 35 dB of the maximum image value. We see four clusters of relative phase values, corresponding to each of the four scattering centers.

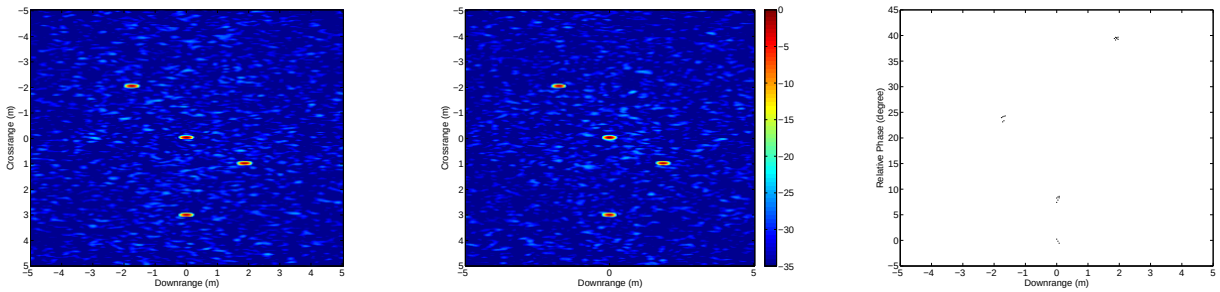

Figure 2. Noisy SAR Slant plane images showing the top 35dB for the two peak elevation angles 29.5 and 29.5714 degrees and the corresponding relative phase plot.

Figure 3 shows the results of independent image enhancement.[2] Specifically, point-enhanced SAR images are obtained using $p = 1$ and $\lambda^2 = 0.8$. The magnitudes of the resulting images are shown in Figure 3. We have used for the termination condition, $\delta_{Ind} = 10^{-4}$, CG tolerance to be $\delta_{CG} = 10^{-3}$ and the approximation parameter in (9) as $\epsilon = 10^{-5}$. It is clear from the relative phase plot in Figure 3 that processing the two images independently degrades the inter-channel information, compared with the polar format algorithm images in Figure 2. The relative phase degradation would result in a similar degradation for scattering center height estimation using equation (4).

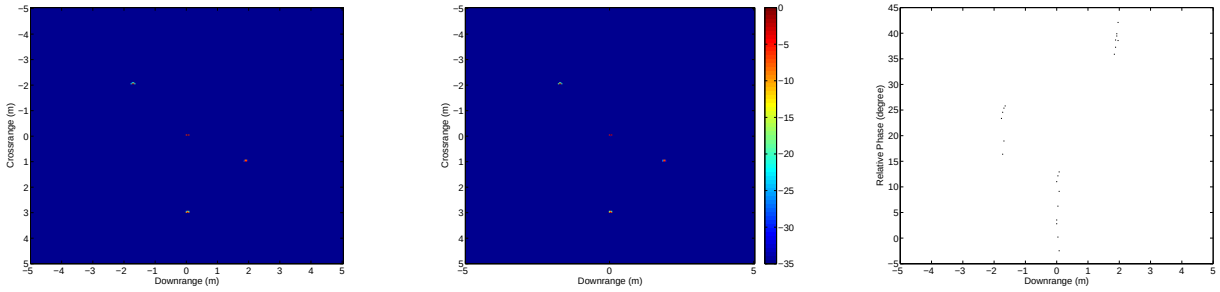

Figure 3. Independently Enhanced SAR Slant plane images showing the top 35dB for the two peak elevation angles 29.5 and 29.5714 degrees and the corresponding relative phase plot.

Figure 4 shows the resulting image and relative phases for the jointly-enhanced image using the procedure in Section 3. Since the magnitudes of both reconstructed images are equal, only a single magnitude image is shown. The images were obtained using the Gradient Descent method, using $\lambda^2 = 0.8$ and $p = 1$ as in the independent enhancement case; we set $\delta = 5\text{x}10^{-3}$ and we have used $\gamma = 10^{-4}$. The Gradient Descent method was slower than the independent enhancement case and required about 40 times the computation of the independent enhancement technique. We also observed that the convergence time for the Gradient Descent method was very sensitive to the choice of δ. The relative phases for this case are considerably less varied than in the independent-enhancement case, and hence would result in lower scattering center height estimation errors in subsequent IFSAR height estimation.

Figure 4. Jointly Enhanced SAR Slant plane images showing the top 35dB for the two peak elevation angles 29.5 and 29.5714 degrees and the corresponding relative phase plot.

The Lagrange-Newton method was computationally more intensive than the conjugate gradient method for this example. However, our implementation does not take advantage of some of the structure inherently present in the matrix M; this structure could be exploited to develop faster algorithms, and is a subject of current research.

5. CONCLUSIONS

We have developed a joint enhancement technique that applies to multiple SAR images of the same scene, such as IFSAR images at closely-spaced elevation angles or multiple polarization images. The enhancement technique is a reconstruction method that simultaneously minimizes a measurement error and imposes a sparsity condition on the reconstructed images.[2,3] While separate enhancement of each image is possible, relative phases of the resulting image pixels is not well-preserved. Relative phases are important for subsequent polarimetric processing or 3D scattering center location estimation via IFSAR processing. We developed a joint reconstruction problem, and derived two iterative algorithms for computing the jointly-enhanced images. Simulation results demonstrate that the jointly-enhanced images retain inter-channel phase information much better than the independently-enhanced method.

The two joint-enhancement algorithms derived are based on the gradient descent and the Lagrange-Newton methods, respectively. The gradient descent method is of smaller size ($3N$ versus $5N$ for joint enhancement of two images), but has linear convergence. The Lagrange-Newton method has quadratic convergence, but is a larger optimization problem. Future work will consider the tradeoffs between the two methods, and will also consider implementations that take better advantage of the structure of the Lagrange-Newton problem.

REFERENCES

1. C. Jakowatz, D. Wahl, P. Eichel, D. Ghiglia, and P. Thompson, *Spotlight-Mode Synthetic Aperture Radar: A Signal Processing Approach*, Kluwer Academic Publishers, Boston, 1996.
2. M. Cetin and R. L. Moses, "SAR imaging from partial-aperture data with frequency-band omissions," in *Algorithms for Synthetic Aperture Radar Imagery XII*, *Proceedings of SPIE* **5808**, 2005.

3. M. Cetin and W. C. Karl, "Feature-enhanced synthetic aperture radar image formation based on nonquadratic regularization," *IEEE Trans. Image Processing* **10**(4), pp. 623–631, 2001.
4. S. F. Degraaf, "SAR imaging via modern 2D spectral estimation methods," *IEEE Trans. Image Processing* **7**, pp. 729–761, 1998.
5. W. G. Carrara, R. S. Goodman, and R. M. Majewski, *Spotlight Synthetic Aperture Radar*, Artech House, Boston, 1995.
6. L. C. Potter and R. L. Moses, "Attributed scattering centers for SAR ATR," *IEEE Trans. Image Processing* **6**, pp. 79–91, 1997.
7. C. Austin and R. L. Moses, "IFSAR processing for 3D target reconstruction," in *Algorithms for Synthetic Aperture Radar Imagery XII*, E. G. Zelnio and F. D. Garber, eds., *Proceedings of SPIE* **5808**, pp. 1–14, 2005.
8. G. H. Golub and C. F. V. Loan, *Matrix Computations*, The Johns Hopkins University Press, Baltimore, MD, 1996.